

Switchable instantaneous frequency measurement by optical power monitoring based on DP-QPSK modulator

Yu-Lin Zhu(朱昱琳), Bei-Lei Wu(武蓓蕾), Jing Li(李晶), Mu-Guang Wang(王目光), Shi-Ying Xiao(肖世莹), and Feng-Ping Yan(延凤平)

Citation: Chin. Phys. B, 2022, 31 (**4**): 044202. DOI: 10.1088/1674-1056/ac40ff
Journal homepage: http://cpb.iphy.ac.cn; http://iopscience.iop.org/cpb

What follows is a list of articles you may be interested in

Color-image encryption scheme based on channel fusion and spherical diffraction

Jun Wang(王君), Yuan-Xi Zhang(张沅熙), Fan Wang(王凡), Ren-Jie Ni(倪仁杰), and Yu-Heng Hu(胡玉衡)
Chin. Phys. B, 2022, 31 (**3**): 034205. DOI: 10.1088/1674-1056/ac1b87

Flexible broadband polarization converter based on metasurface at microwave band

Qi Wang(王奇), Xiangkun Kong(孔祥鲲), Xiangxi Yan(严祥熙), Yan Xu(徐岩), Shaobin Liu(刘少斌), Jinjun Mo(莫锦军), Xiaochun Liu(刘晓春)
Chin. Phys. B, 2019, 28 (**7**): 074205. DOI: 10.1088/1674-1056/28/7/074205

Design of an augmented reality display based on polarization grating

Renjie Xia(夏人杰), Changshun Wang(王长顺), Yujia Pan(潘雨佳), Tianyu Chen(陈天宇), Ziyao Lyu(吕子瑶), Lili Sun(孙丽丽)
Chin. Phys. B, 2019, 28 (**7**): 074201. DOI: 10.1088/1674-1056/28/7/074201

Modulation of energy spectrum and control of coherent microwave transmission at single-photon level by longitudinal field in a superconducting quantum circuit

Xueyi Guo(郭学仪), Hui Deng(邓辉), Hekang Li(李贺康), Pengtao Song(宋鹏涛), Zhan Wang(王战), Luhong Su(苏鹭红), Jie Li(李洁), Yirong Jin(金贻荣), Dongning Zheng(郑东宁)
Chin. Phys. B, 2018, 27 (**7**): 074206. DOI: 10.1088/1674-1056/27/7/074206

Double transmission peaks electromagnetically induced transparency induced by simultaneously exciting the electric and magnetic resonance in one unit cell

Liu Si-Yuan, Zheng Bu-Sheng, Li Hai-Ming, Liu Xiao-Chun, Liu Shao-Bin
Chin. Phys. B, 2015, 24 (**8**): 084204. DOI: 10.1088/1674-1056/24/8/084204

Switchable instantaneous frequency measurement by optical power monitoring based on DP-QPSK modulator

Yu-Lin Zhu(朱昱琳), Bei-Lei Wu(武蓓蕾)†, Jing Li(李晶), Mu-Guang Wang(王目光), Shi-Ying Xiao(肖世莹), and Feng-Ping Yan(延凤平)

Institute of Lightwave Technology, Key Laboratory of All Optical Network and Advanced Telecommunication of EMC, Beijing Jiaotong University, Beijing 100044, *China*

(Received 23 June 2021; revised manuscript received 6 October 2021; accepted manuscript online 8 December 2021)

We propose and analyze an instantaneous frequency measurement system by using optical power monitoring technique with improved resolution. The primary component adopted in the proposal is a dual-polarization quadrature phase shift keying (DP-QPSK) modulator which is used to modulate the microwave signal that has a designed time delay and phase shifting. The generated optical signal is sent to polarization beam splitter (PBS) in DP-QPSK modulator. Owing to the complementary transmission nature of polarization interference introduced by PBS, the frequency information is converted into the optical power and the relationship between the amplitude comparison function (ACF) and microwave frequency to be measured is established. Thus, the frequency of the microwave signal can be easily measured through monitoring the optical powers of the two output ports of the PBS. Furthermore, by adjusting the direct current (DC) biases of the DP-QPSK modulator instead of changing the electrical delay, the measurement range and resolution can be switched. In this paper, the basic principle of the instantaneous frequency measurement system is derived in detail, and simulation has been performed to investigate the resolution, the measurement range, and the influence of imperfection devices. The proposed scheme is wavelength-independent and its measurement range is switchable, which can avoid the laser wavelength drifting problem and thus greatly increasing the system flexibility.

Keywords: microwave photonics, DP-QPSK modulator, instantaneous frequency measurement

PACS: 42.40.My, 42.79.–e, 42.81.–I **DOI:** 10.1088/1674-1056/ac40ff

1. Introduction

Instantaneous frequency measurement (IFM) receiver is an essential component in a modern electronic support measure system, especially in electronic warfare and radio intelligence.[1] Traditional frequency measurement is usually implemented based on electronic devices due to its high resolution and high flexibility. However, for many applications, the microwave measurement that has a relatively large frequency range (from sub-gigahertz to millimeter-wave) is desired, which cannot be achieved by using electronic devices for the limited bandwidth of commercial electronic components.[2] Besides, the electrical frequency measurement suffers bulky size and is sensitive to electromagnetic interference.

Microwave photonic technology provides a solution to the problems mentioned above by offering the advantages of large bandwidth, light weight, low loss, and immunity to electromagnetic interference.[3] In recent years, a variety of photonics-based techniques including frequency–space mapping,[4,5] frequency–time mapping,[6,7] frequency–power mapping[8,9] have been reported. Among them, frequency–power mapping-based method is considered as one of the most common schemes for IFM system. The basic principle of this method is to construct a relationship between the unknown microwave frequency and optical or electric power to perform an amplitude comparison function (ACF) which is the ratio between two different optical or electric power functions. In Refs. [10–12], a dispersion component such as a multichannel chirped fiber Bragg grating, single-mode fiber (SMF), and a dispersion compensating fiber (DCF) is employed to implement the microwave signal power fading and time delay, and the functional relationship between the chromatic dispersion and microwave frequency can be established. By solving the anti-function and monitoring the microwave power, the unknown frequency can be measured. However, for most dispersion-based schemes, high-frequency photo-diode (PD) and electronic devices are required for microwave power detection, which may restrict IFM system by the requirement for low cost.

In order to overcome these limitations, optical power-monitoring methods of measuring the microwave frequency are strongly desired, for only low-speed photodiodes and simple electronics are used now. The key technique of the optical power-monitoring approaches is to use a complementary optical filter pair with specific spectral response to construct two complementary frequency-optical amplitude responses, *i.e.*, the ACF. In Ref. [13], the ACF was established by using the complementary features of the transmission and reflection responses of fiber Bragg grating (FBG). But this scheme encounters a problem about poor long-term stability, for the spectral of FBG is sensitive to temperature. Besides, the wavelength

†Corresponding author. E-mail: wubeilei@bjtu.edu.cn

© 2022 Chinese Physical Society and IOP Publishing Ltd

of the laser should be aligned with the center wavelength of the FBG. Thus, a complex control system needs to stabilize the FBG and the laser wavelength. Similarly, the systems in Refs. [14,15] respectively employed a Mach–Zehnder interferometer with complementary transmission response, a two-tap Sagnac-loop filter with sinusoidal spectral response, and a polarization-maintaining fiber (PMF) to construct the ACF. However, the wavelength drifts of the laser sources and the filter spectral response would result in measuring error due to the mismatch of the wavelength of optical carrier with the valley and peak of the frequency response of the filter. Recently, IFM systems based on an integrated ring-assisted Mach–Zehnder interferometer filter and birefringence effect in the highly nonlinear fiber (HNLF) have been demonstrated[16] to possess the stable filter spectral response, which solves the challenges of wavelength drifts in filter. However, the precise alignment of the laser wavelength is still desired. Besides, the schemes presented in Refs. [14–16] both need the optical filter with specific spectral response, which may make the methods wavelength-dependent and limit the flexibility. The method of using a dual-polarization Mach–Zehnder modulator without optical filter achieves wavelength-independent operation, but it needs an electrical tunable delay line (TDL) for different measurement ranges and resolutions, which has a limited frequency bandwidth and cannot satisfy the requirements for wideband operation for IFM system.

In this paper, we propose an instantaneous microwave frequency measurement system by using optical power monitoring based on dual-polarization quadrature phase shift keying (DP-QPSK) modulator. In the approach, a DP-QPSK modulator is used to modulate the unknown microwave signal with a designed time delay and phase shifting. By using the complementary nature in polarization domain, the microwave frequency information is converted into the optical power and then the ACF is established. Compared with traditional optical power monitoring schemes, the proposed method features wavelength-independent operation, which overcomes the wavelength drifts problem and greatly increases the flexibility. Besides, by adjusting the direct current (DC) biases of the DP-QPSK modulator instead of changing the electrical TDL, the measurement range and resolution can be switched. For the time delay equal to 25 ps, by adjusting the DC biases, the complementary ACF curve of the IFM system can be switched. The measurement range and the resolution can be switched from 0 GHz–10 GHz to 0 GHz–20 GHz and 100 MHz–200 MHz, respectively.

2. Principle

The schematic diagram of the proposed IFM system is shown in Fig. 1, which includes a laser diode (LD), a DP-QPSK modulator, a polarization beam splitter (PBS), a polarization controller (PC), and two optical power monitors (OPM). The light wave is generated by a laser diode (LD) and sent to a DP-QPSK modulator. The DP-QPSK modulator is an integrated device which includes four Mach–Zehnder modulators (MZM1–MZM4), one 90° polarization rotator (PR) and one polarization beam combiners (PBC). The MZM1 and MZM2 are set in parallel, forming the fifth MZM (MZM5). The MZM3 and MZM4 are set in parallel, forming the sixth MZM (MZM6). The MZM5 and MZM6 denote upper arm and lower arm. The unknown microwave signal with angular frequency $\omega_{\rm m} = 2\pi f_{\rm m}$ and an amplitude of $V_{\rm m}$ is split by an RF power splitter to drive the four branches of the DP-QPSK modulator, respectively. In the upper arm, the electrical cables have fixed lengths which will give rise to a designed time mismatching D between the two arms. Besides, two 90° hybrid are used before MZM2 and MZM4 to drive an unknown signal. The lower arm is integrated with a 90° polarization rotator in order to make the optical signals polarized orthogonally. In the DP-QPSK modulator, MZM5 and MZM6 work at the minimum transmission point ($V_{\rm baias} = V_\pi$, where V_π represents the half-wave switching voltage).

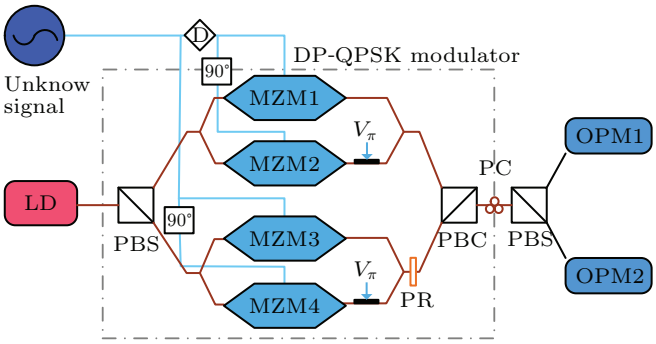


Fig. 1. Schematic diagram of instantaneous frequency measurement, LD: laser diode; PC: polarization controller; D: delay line; MZM: Mach–Zehnder modulator; PBC: polarization beam combiner; PR: polarization rotator; PBS: polarization beam splitter; OPM: optical power monitor.

The optical field from the MZM1–MZM4 is given by

$$\begin{aligned}
E_{\rm MZM1} &= \frac{1}{4}E_{\rm in}\cos\left(\pi\frac{2V_{\rm m}\cos\left(\omega_{\rm m}t+\omega_{\rm m}D\right)+V_{\rm baias}}{2V_\pi}\right)\\
&\quad\times\exp\left({\rm j}\pi\frac{V_{\rm baias}}{2V_\pi}\right),\\
E_{\rm MZM2} &= \frac{1}{4}E_{\rm in}\cos\left(\pi\frac{2V_{\rm m}\sin\left(\omega_{\rm m}t+\omega_{\rm m}D\right)+V_{\rm baias}}{2V_\pi}\right)\\
&\quad\times\exp\left({\rm j}\pi\frac{V_{\rm baias}}{2V_\pi}\right),\\
E_{\rm MZM3} &= \frac{1}{4}E_{\rm in}\cos\left(\pi\frac{2V_{\rm m}\cos\left(\omega_{\rm m}t\right)+V_{\rm baias}}{2V_\pi}\right)\\
&\quad\times\exp\left({\rm j}\pi\frac{V_{\rm baias}}{2V_\pi}\right),\\
E_{\rm MZM4} &= \frac{1}{4}E_{\rm in}\cos\left(\pi\frac{2V_{\rm m}\sin\left(\omega_{\rm m}t\right)+V_{\rm baias}}{2V_\pi}\right)\\
&\quad\times\exp\left({\rm j}\pi\frac{V_{\rm baias}}{2V_\pi}\right).
\end{aligned}\tag{1}$$

The optical field from the upper arm and lower arm can be written as

$$\begin{aligned} E_{\text{upper}} &= \frac{1}{4}E_{\text{in}}\left[\cos\left(\pi\frac{2V_{\text{m}}\cos(\omega_{\text{m}}t+\omega_{\text{m}}D)+V_{\text{baias}}}{2V_\pi}\right)\right. \\ &\quad \left.-\cos\left(\pi\frac{2V_{\text{m}}\sin(\omega_{\text{m}}t+\omega_{\text{m}}D)+V_{\text{baias}}}{2V_\pi}\right)\right] \\ &\quad \times\exp\left(\text{j}\pi\frac{V_{\text{baias}}}{2V_\pi}\right), \\ E_{\text{lower}} &= \frac{1}{4}E_{\text{in}}\left[\cos\left(\pi\frac{2V_{\text{m}}\cos(\omega_{\text{m}}t)+V_{\text{baias}}}{2V_\pi}\right)\right. \\ &\quad \left.-\cos\left(\pi\frac{2V_{\text{m}}\sin(\omega_{\text{m}}t)+V_{\text{baias}}}{2V_\pi}\right)\right] \\ &\quad \times\exp\left(\text{j}\pi\frac{V_{\text{baias}}}{2V_\pi}\right). \end{aligned} \tag{2}$$

The modulated optical signals are combined by a polarization beam combiner (PBC). Then, the output signal from DP-QPSK modulator is sent to a polarization beam splitter (PBS) via a PC. Here, the PC is used to align the output signal's polarization direction at an angle of 45° with respect to the principal axis (E_{upper} and E_{lower}) of PBS. The optical field at the output of PBS at port A and port B are E_{A} and E_{B} and can be expressed as follows:

$$\begin{aligned} E_{\text{A}} &= \frac{1}{\sqrt{2}}\left[E_{\text{upper}}(t)-E_{\text{lower}}(t)\right], \\ E_{\text{B}} &= \frac{1}{\sqrt{2}}\left[E_{\text{upper}}(t)+E_{\text{lower}}(t)\right]. \end{aligned} \tag{3}$$

The two optical power monitors are used to monitor the optical power after PBS. Through the ratio between the two measured power values, the amplitude comparison function (ACF) can be obtained. In this paper, the theoretical analyses of MZM1–MZM4 in different working conditions are carried out.

By adjusting the DC biases of the DP-QPSK modulator (MZM1–MZM4), the measurement range and resolution can be switched. The detailed theoretical analyses of different working conditions are conducted as follows.

Case A When MZM1–MZM4 work at the maximum transmission point ($V_{\text{baias}}=0$ V), equation (2) can be rewritten as

$$\begin{aligned} E_{\text{upper}} &= \frac{1}{4}E_{\text{in}}\left[\cos\left(\pi\frac{V_{\text{m}}\cos(\omega_{\text{m}}t+\omega_{\text{m}}D)}{V_\pi}\right)\right. \\ &\quad \left.-\cos\left(\pi\frac{V_{\text{m}}\sin(\omega_{\text{m}}t+\omega_{\text{m}}D)}{V_\pi}\right)\right], \\ E_{\text{lower}} &= \frac{1}{4}E_{\text{in}}\left[\cos\left(\pi\frac{V_{\text{m}}\cos(\omega_{\text{m}}t)}{V_\pi}\right)\right. \\ &\quad \left.-\cos\left(\pi\frac{V_{\text{m}}\sin(\omega_{\text{m}}t)}{V_\pi}\right)\right]. \end{aligned} \tag{4}$$

Expanding Eq. (4) with the Jacobi–Anger identity and the modulation index is defined as $\varphi=\pi V_{\text{m}}/V_\pi$. Equation (4) can be rewritten as

$$E_{\text{upper}} = -E_{\text{in}}\sum_{n=1}^{\infty}\text{J}_{4n-2}(\varphi)\cos\left(2n(\omega_{\text{m}}t+\omega_{\text{m}}D)\right),$$

$$E_{\text{lower}} = -E_{\text{in}}\sum_{n=1}^{\infty}\text{J}_{4n-2}(\varphi)\cos(2n\omega_{\text{m}}t). \tag{5}$$

Note that only the carrier and the ±2nd sidebands are considered under small-signal modulation condition in Eq. (5). Then the optical field (Eq. (5)) can be rewritten as

$$\begin{aligned} E_{\text{upper}} &= -E_{\text{in}}\text{J}_2(\varphi)\cos\left(2(\omega_{\text{m}}t+\omega_{\text{m}}D)\right), \\ E_{\text{lower}} &= -E_{\text{in}}\text{J}_2(\varphi)\cos(2\omega_{\text{m}}t), \end{aligned} \tag{6}$$

where $\text{J}_2(x)$ is the 2nd-order Bessel function. After PC, the polarization of generated signal rotates an angle of 45°. The optical power at the output of PBS at port A and port B are P_{A} and P_{B}, respectively. Substituting Eq. (6) into Eq. (3), the power which is monitored by the optical power monitors can be obtained as

$$\begin{aligned} P_{\text{A}} &= |E_{\text{in}}\text{J}_2(\varphi)\sin(\omega_{\text{m}}D)|^2, \\ P_{\text{B}} &= |E_{\text{in}}\text{J}_2(\varphi)\cos(\omega_{\text{m}}D)|^2. \end{aligned} \tag{7}$$

Thus, the ratio between the measured power values is given by

$$\text{ACF}=\frac{P_{\text{A}}}{P_{\text{B}}}=\tan^2(\omega_{\text{m}}D). \tag{8}$$

Case B When MZM1–MZM4 work at the minimum transmission point ($V_{\text{baias}}=V_\pi$), equation (2) can be rewritten as

$$\begin{aligned} E_{\text{upper}} &= \frac{\text{j}}{4}E_{\text{in}}\left[-\sin\left(\pi\frac{V_{\text{m}}\cos(\omega_{\text{m}}t+\omega_{\text{m}}D)}{V_\pi}\right)\right. \\ &\quad \left.+\sin\left(\pi\frac{V_{\text{m}}\sin(\omega_{\text{m}}t+\omega_{\text{m}}D)}{V_\pi}\right)\right], \\ E_{\text{lower}} &= \frac{\text{j}}{4}E_{\text{in}}\left[-\sin\left(\pi\frac{V_{\text{m}}\cos(\omega_{\text{m}}t)}{V_\pi}\right)\right. \\ &\quad \left.+\sin\left(\pi\frac{V_{\text{m}}\sin(\omega_{\text{m}}t)}{V_\pi}\right)\right]. \end{aligned} \tag{9}$$

Expanding Eq. (9) with the Jacobi–Anger identity and the modulation index is defined as $\varphi=\pi V_{\text{m}}/V_\pi$. Equation (9) can be rewritten as

$$\begin{aligned} E_{\text{upper}} &= \frac{\text{j}}{2}E_{\text{in}}\sum_{n=1}^{\infty}\text{J}_{2n-1}(\varphi)\left[(-1)^n\cos\left((2n-1)(\omega_{\text{m}}t+\omega_{\text{m}}D)\right)\right. \\ &\quad \left.+\sin\left((2n-1)(\omega_{\text{m}}t+\omega_{\text{m}}D)\right)\right], \\ E_{\text{lower}} &= \frac{\text{j}}{2}E_{\text{in}}\sum_{n=1}^{\infty}\text{J}_{2n-1}(\varphi)\left[(-1)^n\cos\left((2n-1)\omega_{\text{m}}t\right)\right. \\ &\quad \left.+\sin\left((2n-1)\omega_{\text{m}}t\right)\right]. \end{aligned} \tag{10}$$

Under small signal conditions, we consider only the first harmonic ($n=1$) and the modulation index is considered as $\varphi=\pi V_{\text{m}}/V_\pi$. Therefore, the optical field at the output of PBS can be rewritten as

$$E_{\text{upper}} = \frac{\text{j}}{2}E_{\text{in}}\text{J}_1(\varphi)\left[-\cos(\omega_{\text{m}}t+\omega_{\text{m}}D)\right.$$

$$+\sin(\omega_{\rm m}t+\omega_{\rm m}D)],$$
$$E_{\rm lower}=\frac{\rm j}{2}E_{\rm in}{\rm J}_1(\varphi)[-\cos(\omega_{\rm m}t)+\sin(\omega_{\rm m}t)], \quad (11)$$

where $\mathrm{J}_1(x)$ is the 1st-order Bessel function of the first kind. Substituting Eq. (11) into Eq. (3), the optical power at the output of PBS can be obtained as

$$P_{\rm A}=\frac{1}{2}\left|E_{\rm in}{\rm J}_1(\varphi)\sin\left(\frac{\omega_{\rm m}D}{2}\right)\right|^2,$$
$$P_{\rm B}=\frac{1}{2}\left|E_{\rm in}{\rm J}_1(\varphi)\cos\left(\frac{\omega_{\rm m}D}{2}\right)\right|^2. \quad (12)$$

Thus, the ratio between the measured power values, denoted as ACF, is given by

$$\mathrm{ACF}=\frac{P_{\rm A}}{P_{\rm B}}=\tan^2\left(\frac{\omega_{\rm m}D}{2}\right). \quad (13)$$

From Eqs. (7) and (11), the relationship between the optical power ratio and the frequency of unknown microwave signal is obtained. The formula of unknown microwave signal frequency can be obtained below.

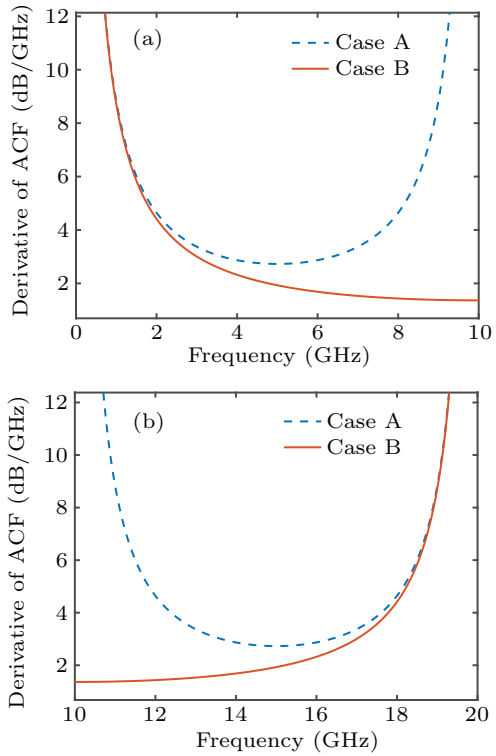


Fig. 2. The first-order derivatives of two ACFs in ranges of (a) 0 GHz–10 GHz and (b) 10 GHz–20 GHz.

The formulas of Case A and Case B are

$$\text{Case A}: f_{\rm m}=\frac{\arctan\left(\sqrt{\mathrm{ACF}}\right)}{2\pi D},\quad\left[0,\frac{1}{4D}\right],$$
$$\text{Case B}: f_{\rm m}=\frac{\arctan\left(\sqrt{\mathrm{ACF}}\right)}{\pi D},\quad\left[0,\frac{1}{2D}\right]. \quad (14)$$

Thus, two methods can be used to achieve IFM in this system. Normally, the measurement range of IFM system is limited to the position of the first notch of the ACF in order to avoid frequency ambiguities. In our scheme, the notch point of the two cases is $1/4D$ and $1/2D$, respectively. The corresponding measurement range for the two cases can be obtained as

$$\text{Case A}\begin{cases}f_{\rm min}=0\ \text{GHz},\\ f_{\rm max}=\dfrac{1}{4D}\ \text{GHz},\end{cases}$$
$$\text{Case B}\begin{cases}f_{\rm min}=0\ \text{GHz},\\ f_{\rm max}=\dfrac{1}{2D}\ \text{GHz}.\end{cases} \quad (15)$$

Then, the resolutions of the two cases are investigated. Since the measurement resolution is directly associated with the absolute value of slope of the ACF curve, in order to acquire a better comprehending of the performance improvement, the absolute values of the first-order derivatives of the ACFs for two cases are compared in 0 GHz–10 GHz and 10 GHz–20 GHz ($D=25$ ps) as shown in Fig. 2.

As can be seen in Figs. 2(a) and 2(b), the absolute value of the first-order derivative of Case A is always higher than that of Case B, which means that Case A has a high resolution than Case B. The theoretically calculated ACF with respect to $D=15$, 20, 25, and 30 ps of two schemes are shown in Figs. 3(a) and 3(b). It can be obtained that the notch point of Case A is $1/4D$ and that of Case B is $1/2D$. Obviously, Case A is more sensitive than Case B.

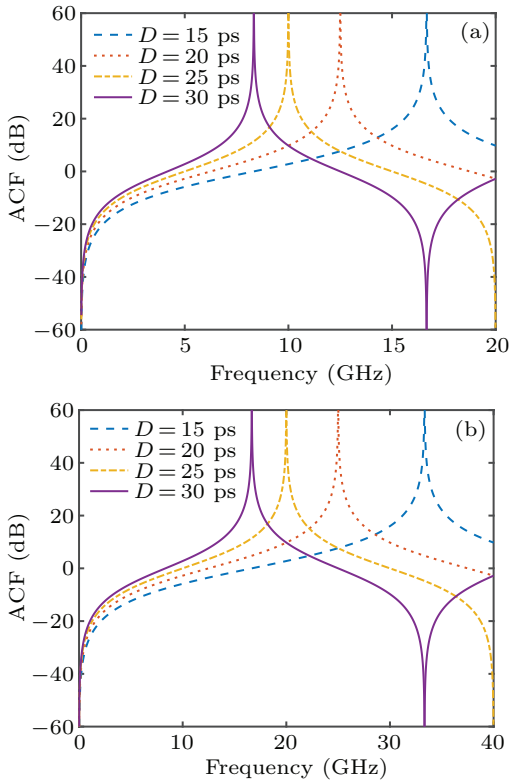


Fig. 3. ACF curves of (a) Case A and (b) Case B at $D=15$ ps, 20 ps, 25 ps, and 30 ps.

According to the above theoretical analysis, a switchable IFM system is proposed. By setting $V_{\rm baias}=V_\pi$, the approximate range of the unknow RF signal can be obtained. Then

V_{baias} is adjusted to 0 V to obtain more accurate measurement frequency. The instantaneous frequency can be calculated from the formula.

3. Simulation

To investigate its mechanism, simulations are preformed by using Optisystem 15.0. The setup is built up as shown in Fig. 1. The frequency of continue wave (CW) laser is 193.1 THz and the linewidth is 10 MHz. Then the laser is injected into a DP-QPSK modulator, which is designed by using a MATLAB program and a programmable module in Optisystem based on its characteristic. In the simulation of Case A, MZM1–MZM4 all work at the maximum transmission point ($V_{baias} = 0$ V) and MZM5 and MZM6 both work at the minimum transmission point ($V_{baias} = V_\pi = 4$ V, V_π represents the half-wave switching voltage). The angle of the principal axis of the PBS with respect to DP-QPSK modulator should be 45°. Then, we use sinusoidal signal as an unknown signal to modulate the DP-QPSK modulator to verify the mechanism of the IFM system.

In order to investigate the laser power-independent characteristic of the scheme, we simulate the optical power curves under different power values of CW laser. By setting $D =$ 25 ps, figure 4(a) shows the optical power curves of P_A and P_B under power of CW laser of 0 dBm and 5 dBm, respectively. Obviously, the curves of P_A and P_B are fully complementary and the difference value between P_A and P_B is identical for different laser power values. The notch points of the curves are both at 10 GHz, which is consistent with the theoretical result. Then by setting $D = 15$, 20, 25, and 30 ps as shown in Fig. 4(b), the simulation results (symboled) are consistent with the theoretical results (line-denoted). It can be obtained that the measurement range is 16.7 GHz, 12.5 GHz, 10 GHz, and 8.3 GHz, respectively, which are consistent with the theoretical results. Taking $D = 25$ ps for example, we compare the theoretical frequency (line-denoted) with the simulation frequency (symboled) as shown in Fig. 4(c). The estimated error is shown in Fig. 4(d). It can be obtained that estimated error is less than 80 MHz when the measurement range is in a range of 0 GHz–10 GHz, which apparently illustrates the validity of proposed IFM system.

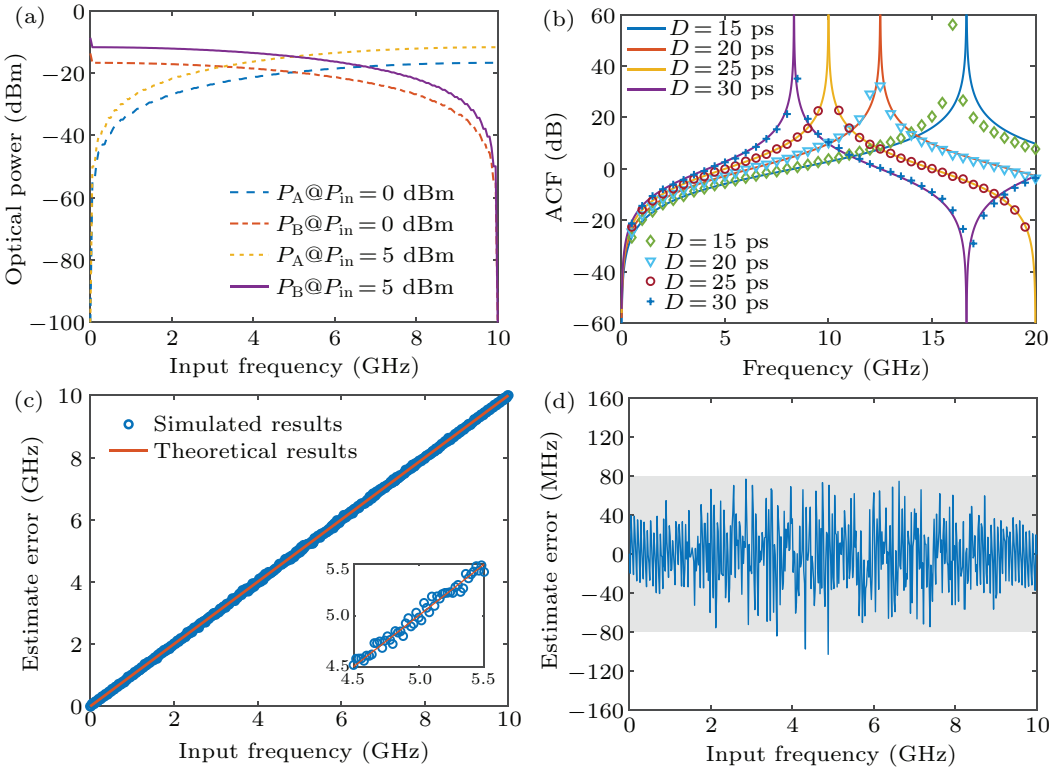


Fig. 4. (a) Simulated curves of optical power (P_A and P_B) *versus* input frequency of Case A at $D = 25$ ps and power values of CW laser $P = 5$ dBm and 0 dBm. (b) Simulated and calculated curves of ACF of Case A at $D = 15$, 20, 25, and 30 ps, with symbols marking simulated results and lines denoting calculated results. (c) Plots of measured frequency (symbol) and theoretical frequency (line) *versus* input frequency of Case A at $D = 25$ ps. (d) Curve of estimated error *versus* frequency of Case A at $D = 25$ ps.

Similarly, by adjusting the DC bias of each MZM ($V_{baias} = V_\pi$), Case B can be simulated and discussed. The optical power curves of P_A and P_B at 0 dBm and 5 dBm, the simulated ACF curves and calculated ACF curves at $D = 15$, 20, 25, and 30 ps as well as the estimated errors are also simulated. As shown in Fig. 5(a), the notch points of the curves are all at 20 GHz, which accords well with the theoretical results. The ACF curves can be obtained when the D values are 15, 20, 25, and 30 ps as shown in Fig. 5(b). The estimated error of the Case B is below 150 MHz and the measured results range

from 0 GHz to 20 GHz as shown in Figs. 5(c) and 5(d). It can be concluded that Case B has a larger measurement range and higher estimated error than Case A.

It is worth noting that there are four factors causing the estimated error in Figs. 4(d) and 5(d). Firstly, in order to simulate the possible influence of the actual environment, we add Gaussian white noise into the simulation. Secondly, the linewidth of the laser is 10 MHz, which will produce many low-order sidebands in the spectrum. Thirdly, the extinction ratio of MZM in the ideal state is infinite, which cannot be achieved in the simulation. Finally, owing to the limited storage space of computer, round-off error will also occur. However, in practice, the limitations induced by the imperfection of components and external environmental factors may also affect the measurable frequency range and accuracy of the proposed system. To optimize the parameter in simulated IFM system, In the following subsections four possible error factors will be discussed and their influences will also be analyzed.

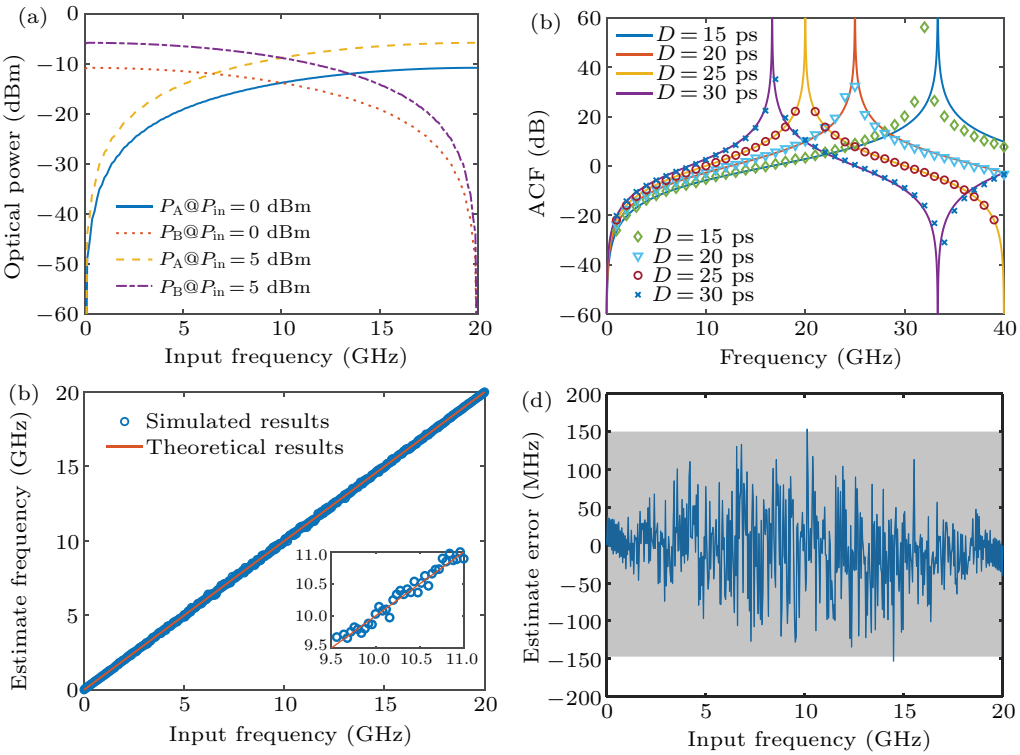


Fig. 5. (a) Simulated curves of optical power (P_A and P_B) *versus* input frequency of Case B at $D = 25$ ps and power of CW laser $P = 5$ dBm and 0 dBm. (b) Simulated and calculated curves of ACF *versus* input frequency of Case B at $D = 15$, 20, 25, and 30 ps, with symbols marking simulated results, and lines denoting calculated results. (c) Plots of measured frequency (marks) and theoretical frequency (line) *versus* input frequency of Case B at $D = 25$ ps. (d) Curve of estimated error *versus* input frequency of Case B at $D = 25$ ps.

3.1. Influence of polarization angle drift

In the proposed system, polarization angle α should be maintained at 45°. In practice, the polarization angle may not exactly be at 45° because of the inaccuracy of the PC or external perturbation, which will weaken performance of the proposed IFM system. We take time delay $D = 25$ ps for example to simulate the shifting of polarization angle. The polarization angle is assumed to be $45° + \Delta\alpha$ ($\Delta\alpha = 0°$, $\pm1°$, $\pm2°$, $\pm3°$, $\pm4°$, and $\pm5°$), where $\Delta\alpha$ represents the polarization angle deviation. The ACF curves and the estimated error curves of Case A are shown in Figs. 6(a) and 6(b) and those of Case B are displayed in Figs. 7(a) and 7(b), respectively. To some extent, the absolute value of ACF curve decreases with the increase of polarization angle drift, especially in the boundary of measurement range, which are shown in Figs. 6(a) and 7(a). The estimated errors are relatively large at 0 GHz and 10 GHz in Case A, which will increase to around $\pm$20 MHz, $\pm$200 MHz, $\pm$450 MHz, $\pm$700 MHz, $\pm$900 MHz, and $\pm$1.15 GHz at $\Delta\alpha = 0°$, $\pm1°$, $\pm2°$, $\pm3°$, $\pm4°$, and $\pm5°$ as shown in Fig. 6(b). To achieve high resolution ($\leq$ 100 MHz) and relatively wide range, $\Delta\alpha$ is supposed to be limited in less than $\pm3°$, where the measurement range will be 0.5 GHz–9.5 GHz as shown in Fig. 6(b). As shown in Fig. 7(b), for Case B, the estimated error is relatively large at 0 GHz and 20 GHz, which will increase to around $\pm$20 MHz, $\pm$100 MHz, $\pm$200 MHz, $\pm$350 MHz, $\pm$450 MHz, and $\pm$550 MHz, at 0°, $\pm1°$, $\pm2°$, $\pm3°$, $\pm4°$, and $\pm5°$. Within the estimated error of 200 MHz, $\Delta\alpha$ should be controlled carefully ($\Delta\alpha \leq \pm3°$), where the measurement range will be 2 GHz–18 GHz as shown in Fig. 7(b). In order to improve the performance of the IFM system, a control circuit can be added to PC through feedback control to improve the accuracy of PC which is relatively expensive. To reduce cost, the polarization maintaining fiber patch cord with a specially designed connector key can be used to set at 45° to replace the PC.[17]

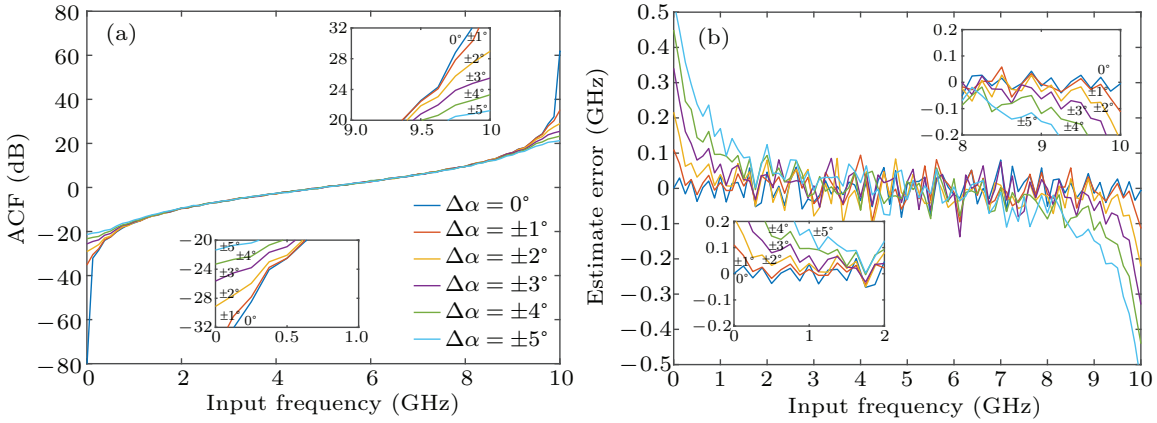


Fig. 6. (a) Curves of ACF *versus* input frequency of Case B at $\Delta\alpha = 0°$, $\pm1°$, $\pm2°$, $\pm3°$, $\pm4°$, and $\pm5°$ and at $D = 25$ ps. (b) Curves of estimated error *versus* input frequency of Case A at $\Delta\alpha = 0°$, $\pm1°$, $\pm2°$, $\pm3°$, $\pm4°$, and $\pm5°$ and at $D = 25$ ps.

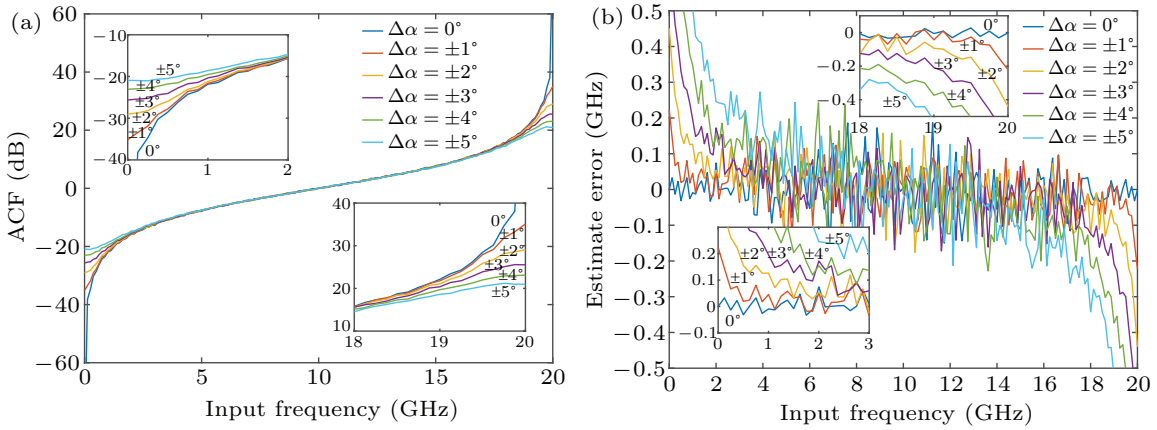


Fig. 7. (a) Curves of ACF *versus* input frequency of Case B at $\Delta\alpha = 0°$, $\pm1°$, $\pm2°$, $\pm3°$, $\pm4°$, and $\pm5°$ and at $D = 25$ ps. (b) Curves of estimated error *versus* input frequency of Case B at $\Delta\alpha = 0°$, $\pm1°$, $\pm2°$, $\pm3°$, $\pm4°$, and $\pm5°$ and at $D = 25$ ps.

3.2. Influence of voltage bias

The variation of external temperature will cause the bias voltage to drift, thereby affecting the ACF curve and narrowing the range of frequency measurement. The bias voltage drift is denoted as ΔV_{baias} and the bias voltage of Case A and Case B are represented by ΔV_{baias} and $V_{\text{baias}} + \Delta V_{\text{baias}}$ respectively. In Mach–Zehnder (MZ) modulator, V_{baias} will be reflected in the output signal in the form of phase shift ($\varphi_1 = \pi V_{\text{baias}}/V_\pi$), so the phase shift angle $\Delta\varphi_1$ can be used to indicate ΔV_{baias} ($\Delta\varphi_1 = \pi\Delta V_{\text{baias}}/V_\pi$). The ACF curves and the estimated error of Case A is shown in Figs. 8(a) and 8(b), while Case B is shown in Figs. 9(a) and 9(b). As shown in Figs. 8(a) and 9(a), the absolute values of ACF curves decrease obviously around the boundary of measurement range. At $\Delta\varphi_1 = 0°$, $\pm2°$, $\pm4°$, $\pm6°$, and $\pm8°$, the estimated errors of Case A are about ±20 MHz, ±200 MHz, ±550 MHz, ±800 MHz, and ±1.05 GHz at the boundary of range, which is shown in Fig. 8(b). The bias voltage can be easily controlled by the bias-voltage control circuit.

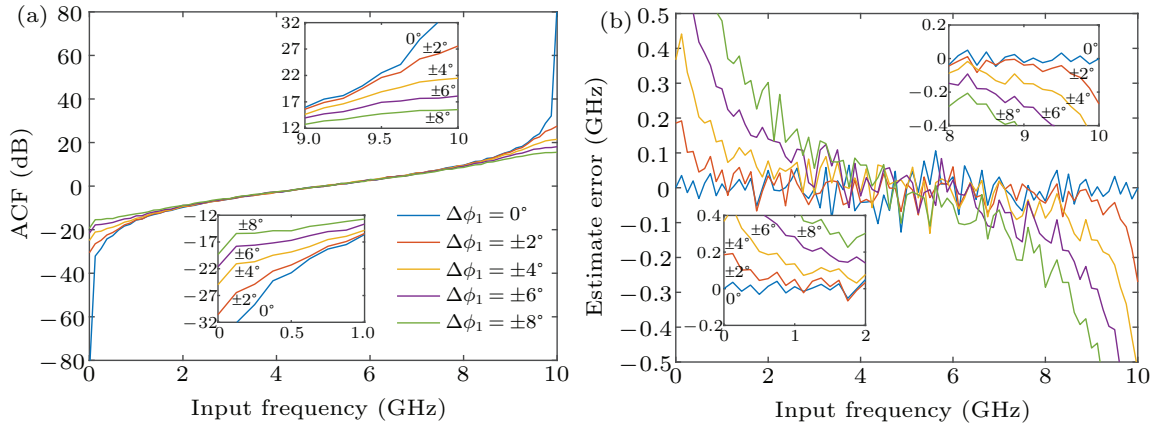


Fig. 8. (a) Curves of ACF *versus* input frequency of Case A at $\Delta\varphi_1 = 0°$, $\pm2°$, $\pm4°$, $\pm6°$, and $\pm8°$ and at $D = 25$ ps. (b) Curves of estimated error *versus* input frequency of Case A at $\Delta\varphi_1 = 0°$, $\pm2°$, $\pm4°$, $\pm6°$, and $\pm8°$ and at $D = 25$ ps.

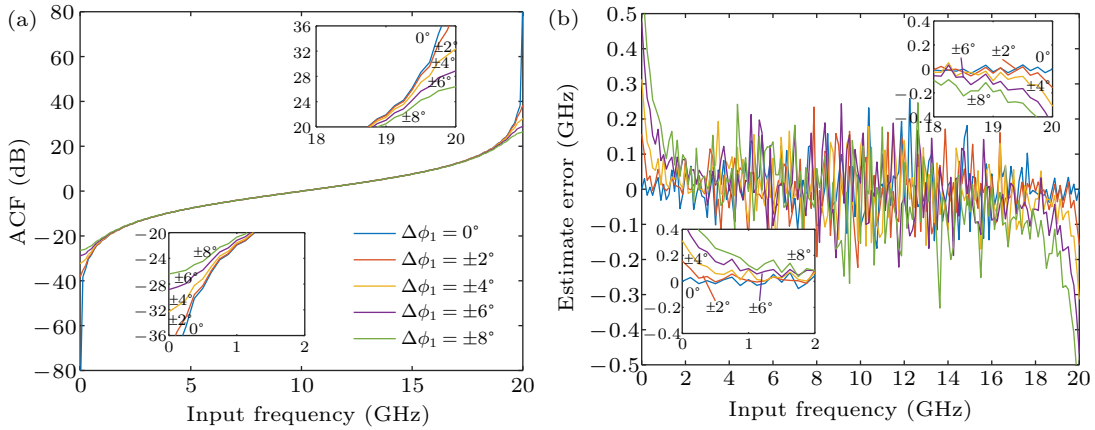


Fig. 9. (a) Curves of ACF *versus* input frequency of Case B at $\Delta\varphi_1 = 0°$, $\pm2°$, $\pm4°$, $\pm6°$, and $\pm8°$ and at $D = 25$ ps. (b) Curves of estimated error *versus* input frequency of Case B at $\Delta\varphi_1 = 0°$, $\pm2°$, $\pm4°$, $\pm6°$, and $\pm8°$ and at $D = 25$ ps.

Within the estimated error below 100 MHz and by using bias-voltage control circuit ($\Delta\varphi_1 \leq 4°$), the measurement range is 1.5 GHz–8.5 GHz in Case A as shown in Fig. 8(b). When the values of $\Delta\varphi_1$ are $0°$, $\pm2°$, $\pm4°$, $\pm6°$, and $\pm8°$, the estimated errors of Case B will reach to around ±20 MHz, ±150 MHz, ±300 MHz, ±450 MHz, and ±500 MHz at the boundary of range, respectively, as shown in Fig. 9(b). By using bias-voltage control circuit ($\Delta\varphi_1 \leq 4°$), the measurement range will be 1 GHz–19 GHz, when the resolution is relatively high (≤ 200 MHz). To suppress the drift of bias voltage, the voltage source can adopt a constant-voltage computerized numerical control (CNC) power supply, and the resolution of the current constant voltage CNC power supply can reach 0.001 V. In our system, the voltage offset less than 0.08 V can meet the system requirements, which means that the constant voltage CNC power supply can be applied to our system.

3.3. Influence of electrical delay line

The electric delay line may affect the measurement range of the IFM system, due to inaccurate delay and microwave signal power attenuation. Aiming at these two effects, the ACF curves and estimated error of the frequency measurement system are simulated and analyzed.

Owing to the limited resolution of the delay line, the time delay may deviate from the expected value. We assume that the time drift is $\Delta\tau$. The simulation of the IFM system is conducted separately at $\Delta\tau = 0$ ps, 0.2 ps, and 0.3 ps is given when we expect $D = 25$ ps. Figures 10(a) and 10(b) display the ACF curves and estimated error of Case A, respectively. Meanwhile, figures 11(a) and 11(b) show the ACF curves and estimated error of Case B. It can be obtained that in Fig. 10(a), the ACF curve deviates to the left or right around 10 GHz with the increase or decrease of time delay. Theoretically, the amplitude of ACF curve will not change. However, owing to the selection of sampling points, the amplitude of ACF curve changes. With high resolution (estimated error ≤ 100 MHz) of Case A, the delay deviation should be within 0.2 ps as shown in Fig. 10(b). Around 20 GHz, ACF curves of Case B shift with the change of time delay as shown in Fig. 11(a). The delay deviation should also be within 0.2 ps with estimated error less than 200 MHz as shown in Fig. 11(b). It can be concluded that the time delay of our proposed system should be carefully controlled. However, the time delay of tunable delay line cannot be accurately calibrated. In our proposed IFM system, electrical cable can be used to introduced fixed time delay. By adjusting working state of DP-QPSK modulator, high resolution in an appropriate measurement range can be achieved.

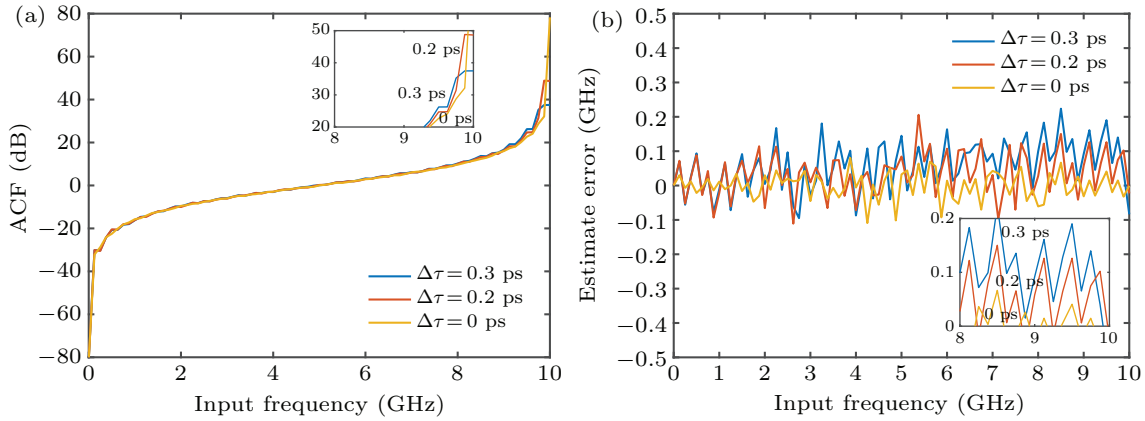


Fig. 10. (a) Curves of ACF *versus* input frequency of Case A at $\Delta\tau = 0.3$ ps, 0.2 ps, and 0 ps at $D = 25$ ps. (b) Curves of estimated error *versus* input frequency of Case A at $\Delta\tau = 0.3$ ps, 0.2 ps, and 0 ps at $D = 25$ ps.

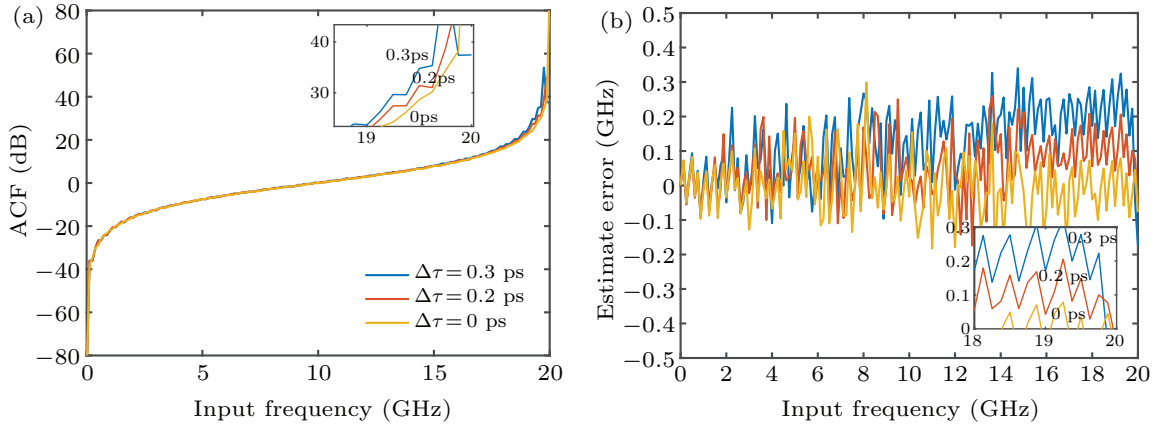


Fig. 11. (a) Curves of ACF *versus* input frequency of Case B at $\Delta\tau = 0.3$ ps, 0.2 ps, and 0 ps at $D = 25$ ps. (b) Curves of estimated error *versus* input frequency of Case A at $\Delta\tau = 0.3$ ps, 0.2 ps, and 0 ps at $D = 25$ ps.

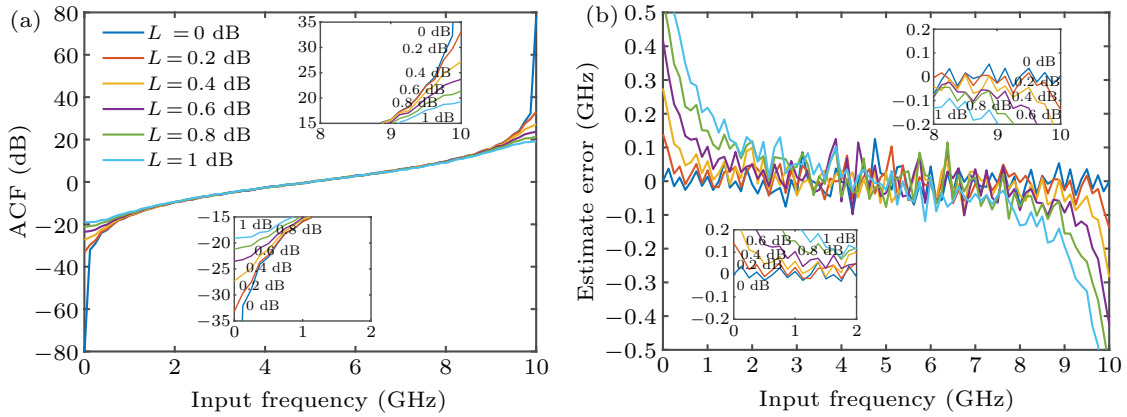


Fig. 12. (a) Curves of ACF *versus* input frequency of Case A at $L = 0$ dB, 0.2 dB, 0.4 dB, 0.6 dB, 0.8 dB, and 1 dB and at $D = 25$ ps. (b) Curves of estimated error *versus* input frequency of Case A at $L = 0$ dB, 0.2 dB, 0.4 dB, 0.6 dB, 0.8 dB, 1 dB and at $D = 25$ ps.

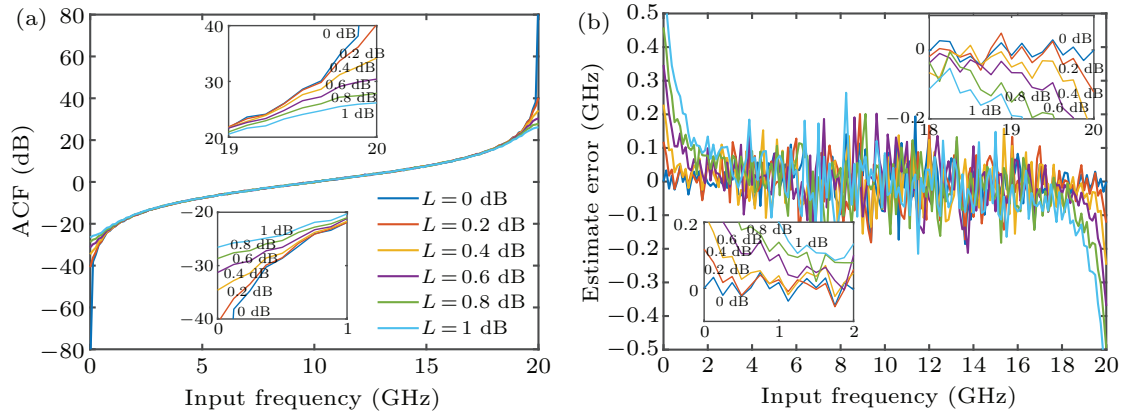


Fig. 13. (a) Curves of ACF *versus* input frequency of Case B at $L = 0$ dB, 0.2 dB, 0.4 dB, 0.6 dB, 0.8 dB, and 1 dB and at $D = 25$ ps. (b) Curves of estimated error *versus* input frequency of Case B at $L = 0$ dB, 0.2 dB, 0.4 dB, 0.6 dB, 0.8 dB, and 1 dB and at $D = 25$ ps.

At the same time, the electric delay line will also cause the power of microwave signal to attenuate. The effect on signal power increases with microwave frequency increasing. When the microwave signal is at 20 GHz, the loss is within 1 dB. By setting the loss of microwave signal to be L, the simulations of the ACF curve and the estimated error are given where $L = 0$ dB, 0.2 dB, 0.4 dB, 0.6 dB, 0.8 dB, 1 dB, and $D = 25$ ps. The ACF curve and estimated error of Case A are shown in Figs. 12(a) and 12(b), and those of Case B are shown in Figs. 13(a) and 13(b). With the increase of the loss, the ACF curve tends to be flat at both ends of 0 GHz and 10 GHz as shown in Fig. 12(a). When $L = 1$ dB, the measurement range of Case A is from 2 GHz to 8 GHz with estimate error less than 0.1 GHz as shown in Fig. 12(b). The trends of ACF curves of Case B are the same at the boundary of measurement range as shown in Fig. 13(a). The measurement range of Case B is from 1 GHz to 19 GHz with estimate error less than 0.2 GHz as shown in Fig. 13(b). It can be obtained from the above analysis that our proposed system can cope with the influence resulting from the increase of delay line loss with the increase

of microwave signal frequency.

3.4. Influence of chirp

There are two sources of chirp in the proposed system, which are the drive signals applied to phase modulator and the finite extinction ratio of the MZM. The influence of modulator chirp effect on frequency measurement system is simulated and analyzed.

In the proposed system, four 180° hybrid couplers will be used to realize push-pull operation. In practice, owing to the component imperfection, there will happen a phase drift in hybrid coupler which will introduce the chirp into MZM. Thus, the influence of hybrid phase balance should be discussed. For example, the electrical time delay is also set to be $D = 25$ ps. The four couplers are identical and the phase drift is $\Delta\beta$. Therefore, the phase difference between two RF ports of each MZM is $180^\circ + \Delta\beta$. We simulate the ACF curve and the estimated error $\Delta\beta = 0^\circ$, $\pm2^\circ$, $\pm4^\circ$, $\pm6^\circ$, and $\pm8^\circ$. The ACF curves and the estimated error curves of Case A are displayed in Figs. 14(a) and 14(b) and those of Case B are displayed in Figs. 15(a) and 15(b). As shown in Figs. 14(a) and 15(a), the ACF curves decrease distinctly around 10 GHz and 20 GHz, respectively, of Case A and Case B. As shown in Fig. 14(b), around 10 GHz, the estimated error of Case A will reach to 20 MHz, 200 MHz, 600 MHz, 800 MHz, and 1.1 GHz, respectively, at $\Delta\beta = 0^\circ$, $\pm2^\circ$, $\pm4^\circ$, $\pm6^\circ$, $\pm8^\circ$. To guarantee that the accuracy of estimated error is less than 100 MHz and the measurement range is relatively feasible, the phase drift should be controlled to be within 4° as shown in Fig. 14(b). In that case, the measurement range of Case A will be 0 GHz–8.5 GHz. Around 20 GHz, the estimated errors of Case B will turn to be around 20 MHz, 100 MHz, 250 MHz, 400 MHz, and 500 MHz, respectively, at $\Delta\beta = 0^\circ$, $\pm2^\circ$, $\pm4^\circ$, $\pm6^\circ$, and $\pm8^\circ$ as shown in Fig. 15(b). For high resolution and relatively feasible measurement range, the phase drift should be controlled to be within 8°, where the measurement range is 0 GHz–19 GHz as shown in Fig. 15(b). The influence of hybrid phase balance can be reduced by precise control, a delay and power tunning component can be added into the input of lower arm to improve the performance.[17]

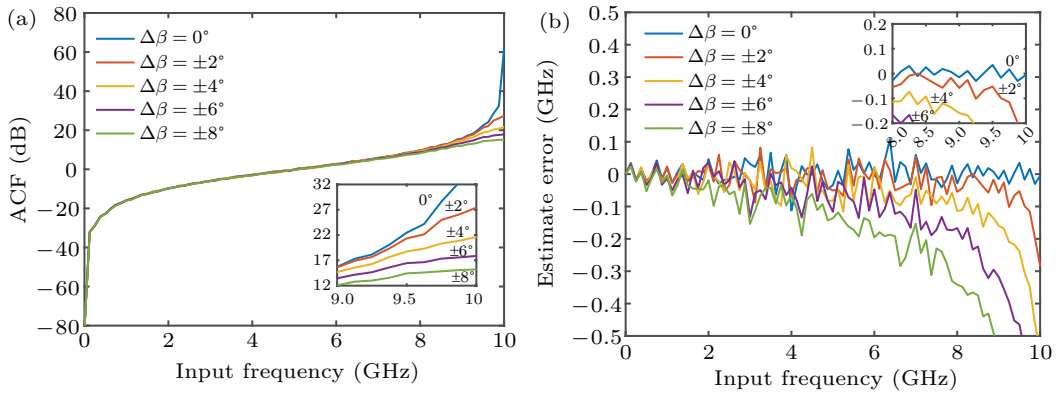


Fig. 14. (a) Curves of ACF input frequency of Case A at $\Delta\beta = 0^\circ$, $\pm2^\circ$, $\pm4^\circ$, $\pm6^\circ$, and $\pm8^\circ$ and at $D = 25$ ps. (b) Curves of estimated error *versus* input frequency of Case A at $\Delta\beta = 0^\circ$, $\pm2^\circ$, $\pm4^\circ$, $\pm6^\circ$, and $\pm8^\circ$ and at $D = 25$ ps.

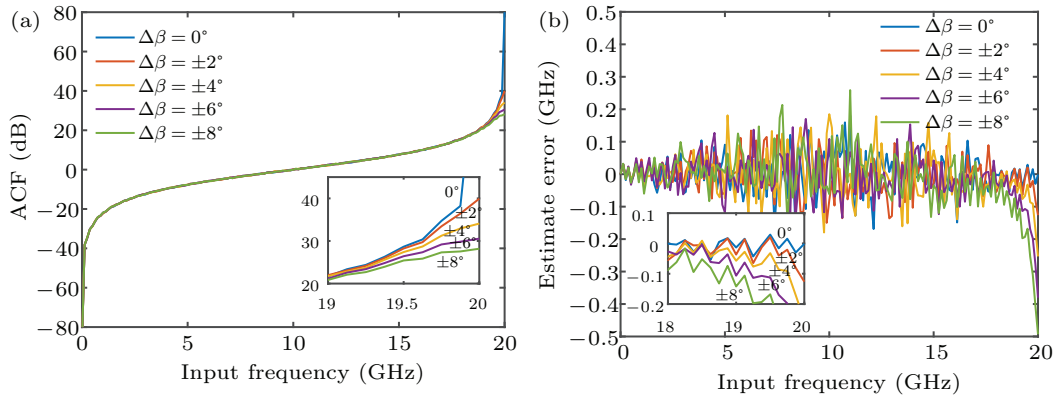


Fig. 15. (a) Curves of ACF *versus* input frequency of Case B at $\Delta\beta = 0^\circ$, $\pm2^\circ$, $\pm4^\circ$, $\pm6^\circ$, and $\pm8^\circ$ and at $D = 25$ ps. (b) Curves of estimated error *versus* input frequency of Case B at $\Delta\beta = 0^\circ$, $\pm2^\circ$, $\pm4^\circ$, $\pm6^\circ$, and $\pm8^\circ$ and at $D = 25$ ps.

Extinction ratio is determined by the properties of modulators which is expect to be infinite. In practice, the finite extinction ratio will cause the optical signal to chip in the system and then make an influence on frequency measurement. The ER represents the value of extinction ratio of IFM. The ACF curves and estimated error of Case A at $D = 25$ ps, ER = 40 dB, 35 dB, 30 dB, 25 dB are shown in Figs. 16(a) and 16(b), respectively. The peaks of ACF curves decrease around

10 GHz as ER decreases, and estimate errors are around 150 MHz, 300 MHz, 500 MHz, 850 MHz, at ER = 40 dB, 35 dB, 30 dB, 25 dB, respectively, as shown in Figs. 16(a) and 16(b). To achieve the high resolution ($\leq$ 100 MHz), the extinction ratio should be above 30 dB and the measurement is in a range from 0 GHz to 9 GHz. Figures 17(a) and 17(b) show the ACF curves and estimated error of Case B, respectively. As shown in Fig. 17(a), the peaks of ACF curves decrease around 20 GHz as ER decreases. The estimated errors are below 200 MHz at ER = 40 dB, 35 dB, 30 dB, 25 dB as shown in Fig. 17(b), which means high resolution ($\leq$ 200 MHz) of Case B can be achieved when ER is above 25 dB. Fortunately, the ER of commercial MZM can reach more than 30 dB.

In this subsection, the theoretical part is verified by simulation. Besides, four possible factors of the inaccuracy of the components in this system are discussed, they being the polarization angle of PBS, the DC bias, the chirp of MZM, and the electrical delay line. The corresponding measures to improve the components performance have been described after analysis, thereby the estimated errors of both Case A and Case B can be restricted in an acceptable boundary ($\leq$ 100 MHz, $\leq$ 200 MHz).

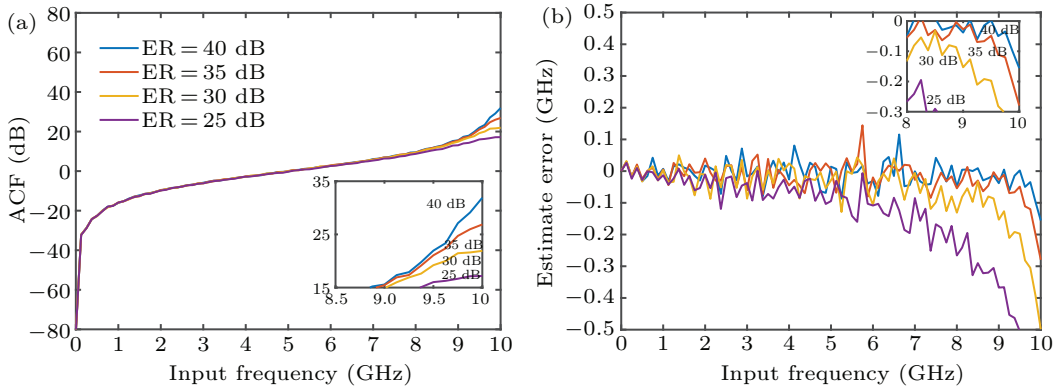


Fig. 16. (a) Curves of ACF *versus* input frequency of Case A at ER = 40 dB, 35 dB, 30 dB, and 25 dB and at $D = 25$ ps. (b) Curves of estimated error *versus* input frequency of Case A at ER = 40 dB, 35 dB, 30 dB, and 25 dB and at $D = 25$ ps.

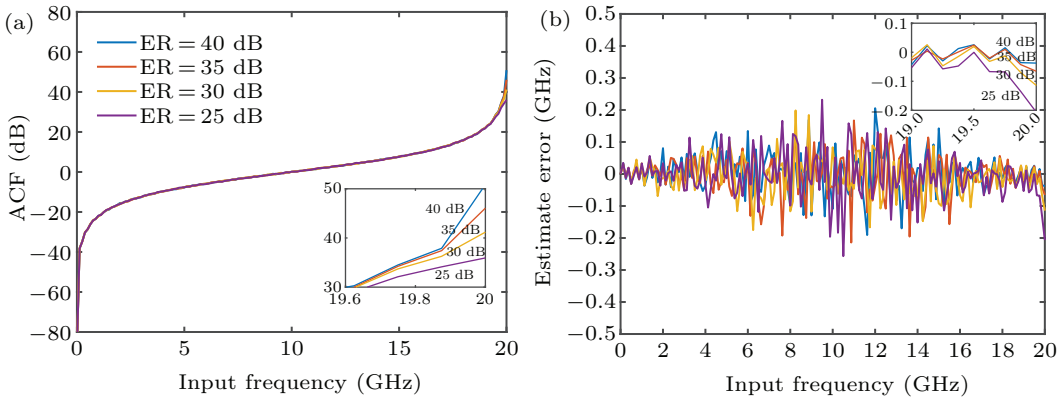


Fig. 17. (a) Curves of ACF *versus* input frequency of Case B at ER = 40 dB, 35 dB, 30 dB, and 25 dB and at $D = 25$ ps. (b) Curves of estimated error *versus* input frequency of Case B at ER = 40 dB, 35 dB, 30 dB, and 25 dB and at $D = 25$ ps.

It is worthy to note that for most of IFM cases, there exists the trade-off issue between the measurement range and resolution, which means that the measurement range needs to be sacrificed in order to obtain a high resolution. In practical applications, a two-step measurement based our proposed scheme can be used to solve this problem. Firstly, as illustrated in Case B, by setting $V_{\text{baias}} = V_\pi$, the IFM with relatively large range ($-1/2D$) is achieved from Eq. (13). If the measurement range is divided into two regions including $-1/4D$ and $1/4D$–$1/2D$, the frequency region of unknown microwave signal can be estimated. Next, by adjusting V_{baias} to 0 V, the IFM with relatively high resolution as shown in Case A is realized. Owing to the symmetry of ACF curve, the measurement range in this case a can be extended to 0 GHz–$1/2D$ GHz. The corresponding formula in this step is

$$f_{\text{m}} = \frac{\arctan\left(\sqrt{\text{ACF}}\right)}{2\pi D}, \quad \left[0, \frac{1}{4D}\right],$$
$$f_{\text{m}} = \frac{1}{2D} - \frac{\arctan\left(\sqrt{\text{ACF}}\right)}{2\pi D}, \quad \left[\frac{1}{4D}, \frac{1}{2D}\right]. \tag{16}$$

Since we can obtain the rough frequency region of the unknown signal from the first step, according to Eq. (18), the more accurate measurement can be achieved. That is to say, the frequency measurement range of the system can reach to $1/2D$, which is determined through the first step, and then the signal frequency can be measured more accurately through the

second step. Thus, our proposed switchable IFM method can solve the trade-off problem and may find applications in future low-cost IFM with both high resolution and large measurement range.

4. Conclusions

In this work, we have proposed an IFM system based on power monitoring by using DP-QPSK modulator. By simply adjusting the DC biases of the DP-QPSK modulator instead of changing the electrical delay, the measurement range and resolution of the system can be switched. The theoretical analysis and the simulation of the IFM system are conducted to display and verify the mechanism. We take $D = 25$ ps for example, by adjusting the DC biases from V_π to 0 V, the measurement range can be extended from 0 GHz–20 GHz to 0 GHz–10 GHz and the resolution can be switched from 150 MHz to 80 MHz. Since the imperfect property of devices may affect the feature of the proposed system, four possible factors of the inaccuracy of the components are discussed, including the polarization angle of PBS, the DC bias of MZM, the chirp of MZM, and the electrical time delay line. It is found that the estimated errors of the system can be limited in an acceptable boundary ($\leq$ 100 MHz) when the property of polarization angle drift, phase shifter and DC bias can be controlled (polarization angle of PC $\Delta\alpha \leq \pm 3^\circ$, phase balance of the MZM $\Delta\beta \leq \pm 4^\circ$, extinction ratio of the MZM ER $\geq$ 30 dB, DC bias of MZM $\Delta\varphi_1 \leq \pm 4^\circ$, delay deviation of TDL $\Delta\tau \leq 0.2$ ps). Compared with the existing IFM method, the optical filter or the high frequency PD is no longer needed in the proposed scheme, which means that the resolution can be higher since it can avoid the measuring error induced by wavelength drifting, electrical noise, and EMI. Besides, the switchable characteristic and no high frequency electrical devices can further increase the flexibility and reduce the cost. Thus, we believe that the proposed architecture can provide a cost-effective and flexible solution for future dynamic microwave frequency measurement.

Acknowledgements

Project supported by the National Natural Science Foundation of China (Grant No. 61801017, U2006217, 62005011, and 61620106014), Beijing Municipal Natural Science Foundation (Grant No. 4212009) and the Fundamental Research Funds for the Central Universities (Grant No. 2020JBM010).

References

[1] Pan S, Zhu D and Zhang F 2014 *Transactions of Nanjing University of Aeronautics and Astronautics* **31** 219
[2] East P W 2012 *IET Radar Sonar Navig.* **6** 112
[3] Seeds A J and Williams K J 2007 *J. Lightwave Technol.* **24** 4628
[4] Winnall S T, Lindsay A C, Austin M W, Canning J and Mitchell A 2006 *IEEE Trans. Microw. Theory Tech.* **54** 868
[5] Wang W S, Davis R L, Jung T J, Lodenkamper R, Lembo L J, Brock J C and Wu M C 2001 *IEEE Trans. Microw. Theory Tech.* **49** 1996
[6] Nguyen L V T 2009 *IEEE Photon. Technol. Lett.* **21** 642
[7] Nguyen T A, Chan E H W and Minasian R A 2014 *Opt. Lett.* **39** 2419
[8] Li W, Zhu N H and Wang L X 2012 *IEEE Photon. J.* **4** 427
[9] Zhang H L and Pan S L 2013 *IEEE Microw. Wirel. Compon. Lett.* **23** 623
[10] Li J Q, Fu S N, Xu K, Zhou J Q, Shum P, Wu J and Lin J T 2009 *Opt. Lett.* **34** 743
[11] Hunter D B and Nguyen L V T 2006 *IEEE Trans. Microw. Theory Tech.* **54** 900
[12] Li Z, Wang C, Li M, Chi H, Zhang X M and Yao J P 2011 *IEEE Microw. Wirel. Compon. Lett.* **21** 52
[13] Dai J A, Xu K, Sun X Q, Niu J A, Lv Q A, Wu J A, Hong X B, Li W and Lin J T 2010 *IEEE Photon. Technol. Lett.* **22** 1162
[14] Chi H, Zou X H and Yao J P 2008 *IEEE Photon. Technol. Lett.* **20** 1249
[15] Feng D Q, Xie H, Qian L F, Bai Q H and Sun J Q 2015 *Opt. Express* **23** 17613
[16] Zheng J Y, Wang H, Li W, Wang L X, Su T, Liu J G and Zhu N H 2014 *Opt. Lett.* **39** 1366
[17] Chen Y and Yao J P 2020 *Journal of Lightwave Technology* **38** 761